submitted to American Mineralogist

Redox-controlled dissolution of monazite in fluids and implications for phase stability in the lithosphere

Dustin Trail[1,2*],

[1]Department of Earth & Environmental Sciences
University of Rochester, Rochester, NY 14627, USA

[2]Department of Earth, Planetary and Space Sciences,
University of California, Los Angeles, CA, USA

* dtrail@ur.rochester.edu; ph 585 276 7182

Submitted 9/6/2017

Revision 1, ms #6296, revised 11/26/17

Keywords: monazite**,** solubility, incongruent dissolution, oxygen fugacity

This is a preprint, the final version is subject to change, of the American Mineralogist (MSA)
Cite as Authors (Year) Title. American Mineralogist, in press.
DOI: http://dx.doi.org/10.2138/am-2018-6296

Abstract

Monazite is an important host of rare earth elements in the lithosphere, including redox-sensitive Ce, which may occur as trivalent and tetravalent in terrestrial environments. Here, monazite solubility is explored as a function of oxygen fugacity through a series of dissolution experiments in alkali-rich and H_2O fluids at 925 ^oC and 1.5 GPa. The oxygen fugacity was controlled with 7 different solid-state buffers, and ranged from about the iron-wüstite to above the magnetite-hematite equilibrium reactions. The solubility of natural monazite increases monotonically at oxygen fugacities equal to or higher than the fayalite-magnetite-quartz equilibrium. Electron microscopy reveals incongruent dissolution at Ni-NiO and above, where Ce-oxide is observed with monazite as a stable phase. Solubility experiments were also conducted with synthetic crystals ($CePO_4$, $LaPO_4$, Th+Si-doped monazite). End-member $CePO_4$ exhibits profound changes to the surface of the crystal under oxidized conditions, with erosion of the crystal surface to depths of ~100 μm or greater, coupled with precipitation of Ce-oxide. In contrast, the solubility of $LaPO_4$ shows no sensitivity to the redox state of the experiment. The addition of Th (~3 wt%) and Si (~0.3 wt%) to monazite promotes crystal stability under oxidizing conditions, though small ThO_2-CeO_2 (5-10 μm) crystals are present on the surfaces of these crystals, whose abundance increases at higher oxygen fugacities. In aggregate, these experiments show that the stability and solubility of monazite is affected by oxygen fugacity, and that the redox state of a fluid may be partially responsible for redistribution of rare earth elements and phosphorus in the crust. Lithospheric fluids with oxygen fugacities at or above the fayalite-magnetite-quartz equilibrium may contribute to some of the complex textures, variable chemistry, and age relationships observed in natural monazite. (279 words)

Introduction

Monazite is a major host of actinide and light rare earth elements (LREEs) in the crust, and is of considerable interest in geochronology because it grows over a broad P/T range in metamorphic terrains (Spear and Pyle 2002; Harrison et al., 2002; Kohn et al., 2004; Catlos, 2013). Thorium oxide (1-10%) and ~1 wt% UO_2 are common components due to high partition coefficients for actinide elements (Stepanov et al. 2012; Xing et al. 2013), though crystal chemistry can be highly variable even within a single grain (Catlos et al., 2002; Pyle and Spear, 2003; Kohn et al., 2004). While monazite is amorphized due to displacive radiation effects, it recovers an ordered structure at relatively low temperatures, and is therefore generally considered to be resistant to radiation damage (Meldrum et al., 1997, 2000). It is also extremely resistant to diffusive loss of U, Th, and Pb from the lattice, with closure temperatures for these elements approaching 900 °C or higher for 10 μm grains and a cooling rate of 10°C/Ma (Cherniak et al. 2004; Cherniak and Pyle, 2008). These properties make monazite a potential host for nuclear waste disposal (e.g., Ewing and Wang, 2002).

Monazite is also utilized as a geothermometer through application of mineral-mineral or mineral-fluid equilibrium reactions. For instance, Pyle et al. (2001) presented trace element partitioning data for monazite, xenotime, and garnet in prograde pelitic rocks, and showed that Y partitioning between garnet and monazite is related to temperature. Plank et al. (2009) suggested that monazite (and allanite) solubility in hydrous silicic fluids can be used to estimate subduction slab temperatures. Principally, this involves a comparison of the temperature-dependent H_2O/Ce ratio in fluids and melts in the presence of a LREE-buffering phases derived from 2.5–4.5 GPa experiments (Hermann and Rubatto, 2009), with the H_2O/Ce of mineral melt inclusions from arc magmas (Plank et al., 2009; Ruscitto et al., 2012; Cooper et al., 2012).

Key to the above applications is the P-T-X dependent stability and solubility of monazite. There are numerous studies which have investigated the alteration, stability, and solubility of monazite as a function of P,T, fluid and/or silicate melt composition (e.g., Ayers and Watson, 1991; Poitrasson et al. 1996; Spear and Pyle, 2002; Ayers et al., 2002; Hermann, 2002; Hermann and Rubatto, 2009; Klimm et al., 2008; Hetherington et al., 2010; Harlov et al., 2011; Budzyn et al., 2011; Skora and Blundy, 2012). Yet, there is no experimental work that has explored the stability and solubility of monazite as a function of oxygen fugacity (fO_2). The goal of this contribution is to help facilitate the interpretation of monazite geochronology and geothermometry, through simple limited-component experiments that assess monazite stability dominantly as a function of oxygen fugacity and monazite chemistry. Experiments reveal a relationship between both these variables.

Experimental strategy and design

Cerium is present as a trivalent and tetravalent cation in natural samples, where the valence is often inferred based on anomalous partitioning of this element compared to La and Pr. For example, zircon LREE patterns often show positive Ce anomalies, reflecting the higher compatibility of Ce^{4+} over Ce^{3+} in the zircon lattice (e.g., Hinton and Upton, 1991; Trail et al., 2012). More direct valence inferences are possible through measurements of Ce valence in experimental or natural samples by X-ray Absorption Near Edge Structure (XANES) spectroscopy (Burnham et al., 2014; Trail et al., 2015). In rare cases, Ce^{4+} exists as a primary component of the mineral formula. Schlüter et al. (2009) identified the mineral stetindite, with an ideal formula of $Ce^{4+}SiO_4$, in the Stetind pegmatite, northern Norway, whereas monazite is expected to contain mostly or only Ce^{3+}. Since Ce is redox sensitive and the most abundant REE in monazite, it is

reasonable to expect that monazite stability and solubility will be influenced by the oxidation state of the system. Experiments were designed to test this hypothesis.

Starting materials

Monazite solubilities vs. f_{O_2} were explored with combination of natural and synthetic crystals. Natural monazite samples consisted of single crystals from the Llallagua tin-porphyry deposit (Bolivia). Llallagua monazite has a mineralization age of ~20 Ma (Kempe et al., 2008; Kohn and Vervoort, 2008), and low actinide concentrations (average U+Th contents ~300 ppm; Catlos and Miller, 2017). Synthetic mm-size monazite crystals were grown by the flux method (e.g., Cherniak and Pyle, 2008) to explore some of the possible changes in mineral solubility as a function of crystal chemistry, and to isolate trivalent from trivalent/tetravalent LREEs. The starting flux mix composition consisted of a ~60 gram mixture of Li_2CO_3-MoO_3. Lithium carbonate and MoO_3 were added in a 1:3 ratio by mole. This was divided into three equal fractions, and to this different monazite starting compositions were mixed. The first and second batches contained respective additions of ~1.5 grams of $LaPO_4 \times H_2O$ or $CePO_4$. The final batch contained 1.5 grams total of $LaPO_4 \times H_2O$ and $CePO_4$ with trace additions of ThO_2 and SiO_2. The latter two components imply the coupled substitution $Th^{4+} + Si^{4+} \leftrightarrow (REE)^{3+} + P^{5+}$, placing the final crystal composition along the monazite-huttonite join. Starting mixes were packed into Pt crucibles, covered with a Pt lid, and suspended in a 1 atm pre-heated vertical tube furnace at ~1350 ^{o}C. The starting material was soaked for ~3 hours, and then cooled to ~900 ^{o}C at a rate of 3^{o}/h. Following synthesis, monazite crystals were freed of residual flux material by ultrasonic cleaning. About half of the experiments were conducted with synthetic phosphates.

Initial characterization of the monazite crystals was carried out with a Photon Machines 193 nm G2 laser ablation (LA) system equipped with a HelEx 2-volume sample chamber connected to an Agilent 7900 inductively coupled plasma mass spectrometer (ICP-MS) quadrupole at the University of Rochester. A laser fluence of 5 J/cm^2 with pulse rate of 10 Hz was used for 15 seconds of total ablation time using a 35 or 50 μm spot. The HelEx 2-volume sample chamber He flow rates were 0.6 liters per minute within the sample chamber (MFC1) whereas the He flow in the HelEx arm was set to 0.2 liters per minute (MFC2). The data were reduced using the Iolite 3.1 software package (Paton, et al., 2011), P was used as an internal standard, and concentrations were calculated by standardizing against NIST610 glass. **Table 1** presents a summary of LA-ICP-MS results, with the averages of measured elements reported. Llallagua monazites typically contain sub-ppm Th and a few hundred ppm of U (single spot data can be found in the supplementary information). These observations are in broad agreement with a recent study that reported chemical information for Llallagua monazites by LA-ICP-MS (Catlos and Miller, 2017).

Experiments

Monazite solubility vs. oxygen fugacity was explored in a 2 N NaOH fluid and in H_2O deionized to a resistivity of 18.2 MΩ·cm with a milli-Q water filtration system. The alkali-rich fluid composition was chosen after the study of Hetherington and Harlov (2008), and after experiments conducted in the same fluid composition reported by Harlov et al. (2011). These workers proposed that altered, metasomatized regions of natural monazite were caused by interactions with alkali-dominated fluids. Single crystals or crystal fragments were dried, carefully weighed, and then placed in Ag or Pt capsules with a known amount of fluid.

Figure 1 presents schematics of the different capsule configurations and the pressure cell. Most of the experiments were conducted in the capsule configuration presented in Figure 1a. The capsule well hosting the monazite has a low profile (~5 mm) and thick wall (~2 mm), which mitigates against thermal gradients and vapor transport/recrystallization of dissolved solutes. In these experiments, the oxygen fugacity was controlled with solid state metal-metal oxide or mineral oxide buffers placed in a separate container (Trail et al., 2012; Figure 1a). The buffer was separated from the monazite-hosted capsule by an H_2 permeable membrane of Pd metal because most buffers are soluble in aqueous solutions at high temperature. In one case, the Ru-RuO_2 buffer – see Figure 1b – was directly added to the capsule because this metal-metal oxide buffer is expected to be insoluble in aqueous solutions at the experiment conditions. Figure 1c presents the configuration for a Ni-NiO buffered experiment. In this case, the Ni metal bucket was oxidized in a muffle furnace at ~1000ºC for 24 h, followed by insertion of Ni+NiO powder and a Pt capsule.

All capsules were pressure sealed with a metal gasket or lid with one of seven solid state f_{O_2} buffers. The f_{O_2} buffers cover a range of 12 log units (**Table 2**). The most reduced experiment was conducted at 4 log units below the fayalite-magnetite-quartz buffer (FMQ-4) while the most oxidized reached ~8 log units above the FMQ equilibrium (Ru-RuO_2). Samples were heated to 925ºC, at a pressure of 1.5 GPa, and the temperature was controlled using calibrated 25%WRe–3%WRe thermocouple wire, with an accuracy of ±3 °C. Pressure was monitored using a 20 cm Heise pressure gauge. The duration for most experiments was ~48 h, though it ranged from 24 to 188 h. These time series experiments were used to evaluate apparent changes in solubility as a function of experiment duration. Experiments were quenched by cutting power to the transformer. The presence of all phases participating in the buffering reaction were verified at the completion of each experiment. Fluid in the buffer chamber (i.e., for designs presented in Figure 1a,c) was

177 also verified. Monazite crystals were removed from the capsules, washed, dried, and re-weighed.
178 Crystals were mounted in epoxy, polished, and imaged using a Zeiss Auriga Scanning Electron
179 Microscope (SEM) to explore the near surface morphologies of heat-treated crystals. Some
180 crystals were placed on carbon tape and imaged with secondary electrons using the same
181 instrument.
182
183 # Results
184 The experimental information, which consists of T,P,t, f_{O_2}, crystal type, fluid composition,
185 and calculated solubilities, is reported in **Table 3**. The percent mass loss to solution is calculated
186 by taking the difference in crystal mass before and after the experiment, and expressing this as a
187 percentage of the total fluid added at the start of the experiment.
188
189 **Natural monazite**
190 Plotting the percent of crystal dissolved in the alkali fluid vs. f_{O_2} shows that Llallagua
191 monazite exhibits higher solubilities for experiments that exceed the FMQ buffer (**Figure 2**). For
192 the 7 experiments conducted at or below the FMQ buffer, the average solubility in the fluid is 0.17
193 ±0.03 wt %. While the lowest recorded solubility among the alkali-rich fluid suite is observed
194 under the most reduced conductions (FMQ-4), a second experiment conducted with the same set
195 of intensive variables yielded values closer to the average solubility calculated for experiments
196 conducted at or below the FMQ buffer. Thus, at oxygen fugacities from FMQ-4 to FMQ, there is
197 no detectable change in the solubility for natural monazites. At FMQ+0.8 (NNO), the first clear
198 evidence for a change in solubility is detected. Experiments more oxidizing than FMQ reveal a
199 monotonic increase in solubility as a function of oxygen fugacity, with a maximum value of ~0.5%

at RRO, which is about 2 log units above the magnetite-hematite buffer. In the most extreme comparison, the solubility of monazite in fluid with fO_2 buffered at the RRO equilibrium is almost 300% higher than experiments buffered at FMQ.

The results of two RRO-buffered experiments presented in Figure 2 were conducted using different capsule configurations. First, the inverted buffer capsule configuration was used, which involved separating the sample chamber from the buffer with Pd foil (e.g. Fig 1a). Because Ru and RuO_2 are both expected to be insoluble in aqueous fluids, these two phases were added directly to the capsule in a second experiment (e.g. Fig. 1b). The statistically identical solubilities provide additional confidence that the buffer readily exchanges H_2 through the Pd membrane to the sample chamber thereby fixing the oxygen fugacity in both chambers. Besides results presented for alkali-rich fluids, a single experiment buffered at RRO in pure H_2O (MD22; 925ºC, 1.5 GPa) yields only a modest solubility (0.03% ±0.02%).

Calculated solubilities do not exhibit a strong dependence on experiment duration (**Figure 3**). For example, FMQ-buffered experiments from 24 to ~200 hours, yield statistically identical solubilities. Thus, solubilities reach a maximum in 24 h or less, consistent with monazite solubility experiments determined by *in situ* techniques (Schmidt et al., 2007). No strong time dependent trends for RRO-buffered experiments are evident, though subtle changes in solubility for the shortest MMO experiment exist (MD14). No evidence for mobility and recrystallization of secondary phases in the bottom of the capsule or along the capsule walls was observed.

Scanning Electron Microscope (SEM) images of natural monazites from alkali-rich fluids, post-experiment, reveal secondary phases indicating incongruent crystal dissolution in some experiments (**Figure 4**). At fO_2s of FMQ+0.8, the monazite is accompanied by small, 2-5 μm britholite-(Ce) crystals, identified by EDS, attached to the surface. At and above the Re-ReO_2

buffer – that is, ≥ FMQ+2.8 – analysis of the images reveals Ce-oxide near the surface, or encased to depths of 5 μm or greater within the monazite. Under the most oxidized conditions (RRO), pervasive alteration of the crystal surface is evident, and the abundance of the Ce-oxide phase is higher. A monazite experiment buffered at RRO in H_2O did not show the same evidence of incongruent dissolution despite the high f_{O_2} imposed.

Synthetic monazite

The relationship between solubility and crystal chemistry vary quite dramatically as a function of f_{O_2} (**Figure 5**). The most soluble synthetic monazite at elevated f_{O_2}s is $CePO_4$, which has implied solubilites – based on weight loss of the crystal – of ~2.5 wt%. Like the trend observed for natural crystals, there is a monotonic increase in solubility from FMQ to RRO. In contrast, synthetic $LaPO_4$ exhibits no change in solubility vs. f_{O_2}. For experiments buffered at FMQ to RRO, the solubilities in the alkali-rich fluid is statistically identical to those reported for natural monazites (~0.17%). Even though the Th+Si-doped crystals contains ~30% Ce, which is comparable to natural Llallagua monazites (Table 2), they show no evidence for elevated solubilities at high f_{O_2}s. For instance, experiments buffered at FMQ and RRO reveal calculated solubilites that are also statistically identical to those obtained for natural samples at oxygen fugacities ≤FMQ. Also, the solubilites are identical to experiments conducted using synthetic $LaPO_4$.

The SEM images of post-experiment synthetic monazites reveal intriguing characteristics (**Figure 6)**. As with natural samples, evidence for incongruent dissolution is present in synthetic $CePO_4$ crystals, though the first appearance of Ce-oxide occurs at the FMQ buffer (compared to FMQ+0.8 for Llallagua monazites). In oxidized fluids (RRO) the dissolution features penetrate to

depths of ~100 μm into the interior of the crystals. Secondary Electron (SE) images of $CePO_4$ reveal convoluted "pillars" of monazite/Ce-oxide attached to the host crystal, that are almost always terminated by Ce-oxide. In contrast, synthetic $LaPO_4$ show no occurrences of La-oxides from FMQ- or RRO-buffered experiments. The Si+Th doped monazite contain distinct crystals of ThO_2-CeO_2 on the surface. The ThO_2-CeO_2 phase forms a solid solution (Whitfield et al., 1966; Aidhy, 2016). When the Si+Th doped crystals are viewed in polished cross section, small sub-μm ThO_2±CeO_2 phases are present in the outer 5 μm of both FMQ- and RRO-buffered experiment products. All features are only found at the termination of the experiment; that is, untreated Si+Th-doped monazite inspected by SEM do not contain ThO_2±CeO_2 phases.

Discussion

The results strongly imply that the mechanism of monazite dissolution varies as a function of crystal chemistry and oxygen fugacity. A few possible reactions are presented as generalizations, but are probably only broadly analogous to those occurring at experimental conditions. One possible dissolution reaction is:

$$(LREEPO_4)_{solid} \leftrightarrow (LREEPO_4)_{aqueous}\ , \qquad (1)$$

which represents congruent dissolution without dissociation, where the constant of this dissolution reaction does not depend on f_{O_2}. This dissolution mechanism was proposed by Rapp and Watson (1986) for silicate melts. This was based on calculated P diffusivities that were nearly identical to the LREEs, suggesting association of these two cations in the melt. Also, consider the reaction:

269

270 $(LREEPO_4)_{solid} \leftrightarrow (LREE^{3+})_{aqueous} + (PO_4^{3-})_{aqueous}$ (2)

271

272 which represents dissolution of dissociated species (e.g., Cetiner et al., 2005). The REE and
273 phosphate ions may also complex with OH and H/Na, respectively (e.g., Devidal et al., 1998;
274 Poitrasson et al., 2004; Cetiner et al., 2005; Pourtier et al., 2010; Tropper et al., 2011), where
275 complexing with OH (e.g., $REE(OH)_3$) may increase the solubility of monazite (Ayers et al.,
276 2004). Given the high activity of OH^- in the starting solution, phosphate ions are probably more
277 likely to complex with Na^+ than H^+. The above possibilities are reasonable approximations for the
278 dominant mechanisms of dissolution for natural monazite crystals from FMQ-4 to ~FMQ. These
279 possibilities also apply, independent of oxygen fugacity, to synthetic crystals comprised of end-
280 member $LaPO_4$.

281 However, the SEM images presented in Figures 4 and 6 show that dissolution can also
282 occur incongruently with changes in oxygen fugacity, monazite chemistry, and fluid composition.
283 A reaction that may occur at f_{O_2}s equal to or above FMQ is:

284

285 $(Ce(OH)_3)_{aqueous} + 0.25O_2 \leftrightarrow (CeO_2)_{solid} + 1.5H_2O$ (3)

286

287 where tetravalent Ce in solid Ce-oxide is inferred based on the lack of evidence for solid REE-
288 oxides at high f_{O_2}s that exclusively occur as trivalent. In other words, the additional solute at high
289 f_{O_2}s is likely to be dominated by $PO_4^{3-}{}_{(aqueous)}$ – with or without Na^+ complexing – given the
290 presence of Ce-oxide in the experimental products. No evidence for reaction (3) is observed for
291 solubility experiments conducted in H_2O (MD22) at elevated f_{O_2}s, highlighting the importance of

292 the NaOH solution. While reaction (3) may explain the presence of CeO_2 and CeO_2-ThO_2 phases,
293 it is not meant to imply that Ce^{4+} complexes are completely insoluble in solution.

294 It is also important to mention that Ce±Th-oxide crystals found on the surface – for
295 example, Fig. 6f,g – do not have morphologies similar to quenched products. In particular, they
296 have well-defined crystal habits and low aspect ratios. Moreover, several examples of CeO_2 and
297 CeO_2-ThO_2 are found encased within the monazite host crystals, which is also evidence that these
298 phases formed during the experiment (Fig. 4c, 6e). The experiments conducted at FMQ with
299 synthetic $CePO_4$ results in a small increase in solubility when compared to the three FMQ
300 experiments conducted on natural crystals. The former experiment also contains CeO_2,
301 demonstrating that Ce^{4+} is present at FMQ.

302 The solubility results obtained for synthetic Th+Si doped monazites (that is, $LaPO_4$ +
303 $CePO_4$ crystals doped with ThO_2 and SiO_2, see Table 2) cannot be completely explained by
304 reactions (1-3). Surface phases of CeO_2-ThO_2 are broadly consistent with reaction (3), but the
305 solubility of monazite in the fluid does not change with f_{O_2} as it does for Llallagua monazites,
306 which have nearly identical Ce concentrations. One crystal chemical difference is that these
307 synthetic monazites do not contain LREEs Pr, Nd, Sm, etc. found in natural monazite. However,
308 this should not result in differences in solubilities as other LREEs are expected to have broadly
309 identical behavior to La. The ~3 wt% Th added to these synthetic crystals is significantly higher
310 than the <100 ppm Th present in the Llallagua crystals; Th may thus impede redox-induced
311 dissolution of monazite. These results are consistent with the observations of Schmidt et al. (2007)
312 whose experiments indicate lower mobility of Th compared LREE. Other studies have also
313 identified Th as a stabilizing component in monazite (Oelkers and Poitrasson 2002; Breiter et al.

2009). Additional experiments in the solid solution ternary $ThSiO_4$-$Ca_{0.5}Th_{0.5}PO_4$-$LREEPO_4$ may help explain this further.

Implications

Hydrothermal alteration of monazite

Solubility studies of accessory minerals have been used to elucidate fluid transport and redistribution of trace elements in the crust (Ayers and Watson, 1991; Ayers and Watson, 1993; Tropper et al., 2011, 2013; Hermann et al., 2013; Budzyń et al., 2013). However, most experimentally determined solubilities of monazite in aqueous fluids are typically very low over a wide range of hydrothermal, metamorphic, and igneous conditions (e.g., Rapp and Watson, 1986; Devidal et al., 1998; Poitrasson et al., 2004; Cetiner et al., 2005; Schmidt et al., 2007; Tropper et al., 2011, 2013; Pourtier et al., 2010).

This contrasts with field observations, where monazite often contains complex zoning that develops in response to fluid alteration. Cherniak and Pyle (2008) documented "perforated" rims in hydrothermally altered monazite, from the amphibolite facies quartzofeldspathic gneiss from the SE Pennsylvania, and Hetherington and Harlov, (2008) observed partially metasomatized monazite megacrysts from granite that contained thorite and uraninite inclusions. Many other examples of destabilized crystal surfaces, patchy zoning, and subsurface inclusions have been documented in natural monazites (e.g., Poitrasson et al., 1996, 2000; Rolland et al., 2003; Ayers et al., 2006; Hetherington and Harlov, 2008; Crowley et al. 2008; Bosse et al., 2009; Harlov and Hetherington, 2010; Kelly et al. 2012; Janots et al. 2012; Seydoux-Guillaume et al., 2012).

A major, first order implication of this work is that monazite stability and solubility are sensitive to the fO_2 of the fluid, and consequently the mobility of P and LREEs in the crust may be

profoundly affected by these fluids under certain conditions. The formation of residual Ce-oxide under oxidizing conditions results in excess PO_4^{3-} in solution. In simple systems, analogous to the experiments presented here, the phosphate concentration will thus be higher, and P more mobile in oxidized environments. In more complex systems, additional phosphate ions in solution due to dissolution of monazite in oxidized fluids may result in the formation or growth of other phosphate phases, such as apatite. The connection between fluid oxidation state and the stability of monazite has also been made in natural samples by Ayers et al. (2013), who argued that the stability of monazite in the country rock of the Searchlight Pluton, Southern Nevada was adversely affected by interaction with oxidized fluids.

Experiments were conducted in H_2O and 2N NaOH fluids, where only the latter resulted in incongruent dissolution under oxidized conductions, so the fluid composition must also be important. The alkali fluid used here may be common in some scenarios (Hetherington and Harlov 2008; Harlov et al. 2011), though alkali-halide brines and temperature may also play a prominent role in oxide and phosphate dissolution reactions (e.g., Ayers and Watson, 1991; Rapp et al., 2010; Tropper et al., 2011; 2013), and are thus worth evaluating in fO_2-buffered experiments as well.

Geochronology

Hydrothermal alteration of monazite has received continued attention because of concerns over how it will affect U–Th–Pb ages (e.g., Poitrasson et al., 1996; Harlov et al., 2011; Williams et al., 2011; Grand'Homme et al., 2016). Experiments conducted with synthetic Th+Si doped monazite contain ThO_2-CeO_2 inclusions on the surface. While the weight loss differences of Th+Si doped monazite experiments could not discern the difference in solubility for FMQ and RRO-buffered experiments, the occurrence of ThO_2-CeO_2 inclusions on the surfaces of the crystal is

more common at elevated oxygen fugacties (e.g., RRO). In some experimental products, ThO_2 and Ce-oxide appears encapsulated as inclusions within the original monazite in 2D sections (e.g., Fig.4c, Fig. 6e). These phases are absent in pre-treated crystals and therefore develop during the experiments. This transport is not possible by lattice diffusion because the diffusivities of tetravalent cations in monazite are too low (e.g., Cherniak and Pyle, 2008) and therefore must be related to a dissolution–reprecipitation migration front through the crystal. Such observations may partially explain why monazites have complicated ages patterns, where interior domains may yield younger ages than the rims of crystals (e.g., Catlos, 2013). In settings with high silica activity, the Th-rich oxides documented here would likely react to form thorite (Hetherington and Harlov 2008; Harlov et al., 2011) or huttonite. Monazite compositions closer the huttonite end-member of the join may form in more oxidizing environments. Furthermore, huttonite may contain Ce^{4+}, the concentration of which is likely to be a function of the oxygen fugacity at the time of crystallization.

Repository for radioactive waste

The ability of monazite to incorporate a range of other actinide elements such as Pu, Am, Cm, Bk, Cf, and Es, while not accumulating lattice damage due to radioactive decay, has led to the suggestion that monoclinic phosphates may be ideal for nuclear waste storage (e.g., Ewing and Wang 2002; Montel et al., 2006; Dacheux et al., 2013). The results of this study show that oxidizing fluids can induce significant dissolution-reprecipitation and the occurrence of secondary phases, the magnitude of which broadly depends on the abundance of multivalent Ce in the monazite structure. Importantly, $LaPO_4$ is not more susceptible to oxidizing fluids. In a study by Veilly et al. (2008) rates of monazite dissolution increased by about two orders of magnitude when

385 multivalent U^{4+} was added to the monazite in place of Th^{4+}. The decrease of chemical durability
386 could be due to the oxidation of U^{4+} to some U^{6+} aqueous species at the solid-solution interface,
387 resulting in weakening of the lattice (Veilly et al., 2008). The effects observed for Th-doped
388 crystals broadly agree with the observations made here.
389

390 ## Acknowledgements

391 Yanling Wang and Jacob Buettner and are thanked for assistance. The LA-ICP-MS instrument at
392 the University of Rochester is partially supported by a grant from the Instrumentation and Facilities
393 Program, Division of Earth Sciences, NSF (EAR-1545637).
394

395 ## References Cited

396 Aidhy, D.S. (2016) Oxygen diffusion in ThO2-CeO2 and ThO2-UO2 solid solutions from
397 atomistic calculations. Physical Chemistry Chemical Physics, 18, 15019-15024.
398 Ayers, J.C., and Watson, E.B., (1991) Solubility of Apatite, Monazite, Zircon, and Rutile in
399 Supercritical Aqueous Fluids with Implications for Subduction Zone Geochemistry.
400 Philosophical Transactions of the Royal Society A: Mathematical, Physical and
401 Engineering Sciences, 335, 365-375.
402 Ayers, J.C., Brenan, J.M., Watson, E.B., Wark, D.A., and Minarik, W.G. (1992) A new capsule
403 technique for hydrothermal experiments using the piston-cylinder apparatus. American
404 Mineralogist, 77, 1080-1086.
405 Ayers, J.C., and Watson, E.B. (1993) Rutile solubility and mobility in supercritical aqueous fluids.
406 Contributions to Mineralogy and Petrology, 114, 321-330.

Ayers, J.C., Crombie, S., Loflin, M., Miller, C.F., and Luo, Y. (2013) Country rock monazite response to intrusion of the Searchlight pluton, southern Nevada: American Journal of Science, 313, 345-394.

Ayers, J.C., Loflin, M., Miller, C.F., Barton, M.D., and Coath, C.D. (2006) In situ oxygen isotope analysis of monazite as a monitor of fluid infiltration during contact metamorphism: Birch Creek Pluton aureole, White Mountains, eastern California. Geology, 34, 653-656.

Bosse, V., Boulvais, P., Gautier, P., Tiepolo, M., Ruffet, G., Devidal, J.L., Cherneva, Z., Gerdjikov, I., and Paquette, J.L. (2009) Fluid-induced disturbance of the monazite Th–Pb chronometer: In situ dating and element mapping in pegmatites from the Rhodope (Greece, Bulgaria). Chemical Geology, 261, 286-302.

Breiter, K., Copjakova, R., and Skoda, R. (2010) The involvement of F,CO2, and As in the alteration of Zr-Th-REE bearing accessory minerals in the Hora Svate Kateriny A-type granite, Czech Republic. The Canadian Mineralogist, 47, 1375-1398.

Budzyn, B., Harlov, D.E., Williams, M.L., and Jercinovic, M.J. (2011) Experimental determination of stability relations between monazite, fluorapatite, allanite, and REE-epidote as a function of pressure, temperature, and fluid composition. American Mineralogist, 96, 1547-1567.

Burnham, A.D., and Berry, A.J., (2014) The effect of oxygen fugacity, melt composition, temperature and pressure on the oxidation state of cerium in silicate melts. Chemical Geology, 366, 52-60.

Catlos, E.J. (2013) Versatile Monazite: resolving geological records and solving challenges in materials science: Generalizations about monazite: Implications for geochronologic studies. American Mineralogist, 98, 819-832.

Catlos, E.J., Gilley, L.D., and Harrison, T.M. (2002) Interpretation of monazite ages obtained via in situ analysis. Chemical Geology, 188, 193– 215.

Catlos, E.J., and Miller, N.R. (2017) Speculations Linking Monazite Compositions to Origin: Llallagua Tin Ore Deposit (Bolivia). Resources, 6, 36. 1-18

Cetiner, Z.S., Wood, S.A., and Gammons, C.H. (2005) The aqueous geochemistry of the rare earth elements. Part XIV. The solubility of rare earth element phosphates from 23 to 150 °C. Chemical Geology, 217, 147-169.

Cherniak, D.J., and Pyle, J.M. (2008) Th diffusion in monazite. Chemical Geology, 256, 52-61.

Cherniak, D.J., Watson, E.B., Grove, M., and Harrison, T.M. (2004) Pb diffusion in monazite: a combined RBS/SIMS study. Geochimica et Cosmochimica Acta, 68, 829-840.

Crowley, J.L., Brown, R.L., Gervais, F., and Gibson, H.D. (2008) Assessing Inheritance of Zircon and Monazite in Granitic Rocks from the Monashee Complex, Canadian Cordillera. Journal of Petrology, 49, 1915-1929.

Dacheux, N., Clavier, N., and Podor, R. (2013) Monazite as a promising long-term radioactive waste matrix: Benefits of high-structural flexibility and chemical durability. American Mineralogist, 98, 833-847.

Devidal, J.-L., Gilbert, F., Kieffer, B., Pin, C., and Montel, J.-M., (1998) A new method for solubility measurement: application to NdPO4 system in H2O-NaCl-HCl hydrothermal fluids. Mineralogical Magazine, 62A, 375-376.

Ewing, R.C., and Wang, L., (2002) Phosphates as Nuclear Waste Forms. Reviews in Mineralogy and Geochemistry, 48, 673-699.

451 Grand'Homme, A., Janots, E., Seydoux-Guillaume, A.-M., Guillaume, D., Bosse, V., and Magnin,
452 V. (2016) Partial resetting of the U-Th-Pb systems in experimentally altered monazite:
453 Nanoscale evidence of incomplete replacement. Geology, 44, 431-434.
454 Harlov, D.E., and Hetherington, C.J. (2010) Partial high-grade alteration of monazite using alkali-
455 bearing fluids: Experiment and nature. American Mineralogist, 95, 1105-1108.
456 Harlov, D.E., Wirth, R., and Hetherington, C.J. (2011) Fluid-mediated partial alteration in
457 monazite: the role of coupled dissolution–reprecipitation in element redistribution and
458 mass transfer. Contributions to Mineralogy and Petrology, 162, 329-348.
459 Harrison, T.M., Catlos, E.J., and Montel, J.-M. (2002) U-Th-Pb dating of phosphate minerals.
460 Reviews in Mineralogy and Geochemistry, 48, 524-558.
461 Hermann, J., and Rubatto, D. (2009) Accessory phase control on the trace element signature of
462 sediment melts in subduction zones. Chemical Geology, 265, 512-526.
463 Hermann, J., Zheng, Y.F., and Rubatto, D. (2013) Deep Fluids in Subducted Continental Crust.
464 Elements, 9, 281-287.
465 Hetherington, C.J., and Harlov, D.E. (2008) Metasomatic thorite and uraninite inclusions in
466 xenotime and monazite from granitic pegmatites, Hidra anorthosite massif, southwestern
467 Norway: Mechanics and fluid chemistry. American Mineralogist, 93, 806-820.
468 Hetherington, C.J., Harlov, D.E., and Budzyń, B. (2010) Experimental metasomatism of monazite
469 and xenotime: mineral stability, REE mobility and fluid composition. Mineralogy and
470 Petrology, 99, 165-184.
471 Hinton, R., and Upton, B.G.J (1991) The chemistry of zircon: Variations within and between large
472 crystals from syenite and alkali basalts. Geochimica et Cosmochimica Acta, 55, 3287-
473 3302.

474 Holland, T.J.B., (1980) The reaction albite = jadeite + quartz determined experimentally in the
475 range 600 to 1200oC. American Mineralogist, 65, 129-134.
476 Janots, E., Berger, A., Gnos, E., Whitehouse, M., Lewin, E., and Pettke, T. (2012) Constraints on
477 fluid evolution during metamorphism from U–Th–Pb systematics in Alpine hydrothermal
478 monazite. Chemical Geology, 326-327, 61-71.
479 Kelly, N.M., Harley, S.L., Möller, A. (2012) Complexity in the behavior and recrystallization of
480 monazite during high-T metamorphism and fluid infiltration. Chemical Geology, 322-
481 323, 192-208.
482 Kempe, U., Lehmann, B., Wolf, D., Rodionov, N., Bombach, K., Schwengfelder, U., and Dietrich,
483 A. (2008) U–Pb SHRIMP geochronology of Th-poor, hydrothermal monazite: An
484 example from the Llallagua tin-porphyry deposit, Bolivia. Geochimica et Cosmochimica
485 Acta, 72, 4352-4366.
486 Klimm, K., Blundy, J.D., and Green, T.H. (2008) Trace Element Partitioning and Accessory Phase
487 Saturation during H2O-Saturated Melting of Basalt with Implications for Subduction
488 Zone Chemical Fluxes. Journal of Petrology, 49, 523-553.
489 Kohn, M.J., and Malloy, M.A., (2004) Formation of monazite via prograde metamorphic reactions
490 among common silicates: implications for age determinations. Geochimica et
491 Cosmochimica Acta, 68, 101-113.
492 Kohn, M.J., and Vervoort, J.D. (2008) U-Th-Pb dating of monazite by single-collector ICP-MS:
493 Pitfalls and potential. Geochemistry, Geophysics, Geosystems 9, 10.1029/2007GC001899
494 Meldrum, A., Boatner, L.A., and Ewing, R.C. (1997) Displacive radiation effects in the monazite-
495 and zircon-structure orthophosphates. Physical Review, B 56, 13,805–13,813.

Meldrum, A., Boatner, L.A., Ewing, R.C., (2000) A comparison of radiation effects in crystalline ABO4 -type phosphates and silicates. Mineralogical Magazine, 64, 185–194.

Montel, J.-M., Glorieux, B., Seydoux-Guillaume, A.-M., and Wirth, R. (2006) Synthesis and sintering of a monazite–brabantite solid solution ceramic for nuclear waste storage. Journal of Physics and Chemistry of Solids, 67, 2489-2500.

Myers, J., and Eugster, H.P., (1983) The System Fe-Si-O: Oxygen Buffer Calibrations to 1,500K. Contributions to Mineralogy and Petrology, 82, 75-90.

Oelkers, E.H., and Poitrasson, F., (2002) An experimental study of the dissolution stoichiometry and rates of a natural monazite as a function of temperature from 50 to 230 oC and pH from 1.5 to 10. Chemical Geology, 191, 73– 87.

O'Neill, H.S.C. (1986) Mo-MoO2 (MOM) oxygen buffer and the free energy of formation of MoO2. American Mineralogist, 71, 1007-1010.

O'Neill, H.S.C. (1987) Quartz-fayalite-iron and quartz-fayalite-magnetite equilibria and the free energy of formation of fayalite (Fe2SiO4) and magnetite (Fe3O4). American Mineralogist, 72, 67-75.

O'Neill, H.S.C., and Nell, J. (1997) Gibbs free energies of formation of RuO2, lrO2, and OsO2: A high-temperature electrochemical and calorimetric study. Geochimica et Cosmochimica Acta, 61, 5279-5293.

O'Neill, H.S.C., and Pownceby, M.I. (1993) Thermodynamic data from redox reactions at high temperatures. I. An experimental and theoretical assessment of the electrochemical method using stabilized zirconia electrolytes, with revised values for the Fe - "FeO", Co-CoO, Ni - NiO and Cu- Cu2O oxygen buffers, and new data for the W-WO2 buffer. Contributions to Mineralogy and Petrology, 296-314.

519 Paton, C., Hellstrom, J., Paul, B., Woodhead, J., and Hergt, J. (2011) Iolite: Freeware for the
520 visualisation and processing of mass spectrometric data. Journal of Analytical Atomic
521 Spectrometry, 26, 2508-2518.
522 Plank, T., Cooper, L.B., and Manning, C.E. (2009). Emerging geothermometers for estimating
523 slab surface temperatures. Nature Geoscience, 2, 611-615.
524 Poitrasson, F., Chenery, S., and Bland, D.J., (1996) Contrasted monazite hydrothermal alteration
525 mechanisms and their geochemical implications. Earth and Planetary Science Letters, 145,
526 79-96.
527 Poitrasson, F., Chenery, S., and Shepherd, T.J. (2000) Electron microprobe and LA-ICP-MS study
528 of monazite hydrothermal alteration: Implications for U-Th-Pb geochronology and
529 nuclear ceramics. Geochimica et Cosmochimica Acta, 64, 3283–3297.
530 Poitrasson, F., Oelkers, E., Schott, J., and Montel, J.-M. (2004) Experimental determination of
531 synthetic NdPO4 monazite end-member solubility in water from 21°C to 300°C:
532 implications for rare earth element mobility in crustal fluids. Geochimica et
533 Cosmochimica Acta, 68, 2207-2221.
534 Pourtier, E., Devidal, J.-L., and Gibert, F. (2010) Solubility measurements of synthetic neodymium
535 monazite as a function of temperature at 2 kbars, and aqueous neodymium speciation in
536 equilibrium with monazite. Geochimica et Cosmochimica Acta, 74, 1872-1891.
537 Pownceby, M.I., and O'Neill, H.S.C. (1994) Thermodynamic data from redox reactions at high
538 temperatures. IV. Calibration of the Re-ReO2 oxygen buffer from EMF and NiO + Ni-
539 Pd redox sensor measurements. Contributions to Mineralogy and Petrology, 118, 130-
540 137.

Pyle, J.M., Spear, F.S., (2003) Four generations of accessory-phase growth in low-pressure migmatites from SW New Hampshire. American Mineralogist, 88, 338–351.

Pyle, J.M., Spear, F.S., Rudnick, R.L., and McDonough, W.F. (2001) Monazite–xenotime–garnet equilibrium in metapelites and a new monazite–garnet thermometer. Journal of Petrology, 42, 2083-2107.

Rapp, R.P., and Watson, E.B. (1986) Monazite solubility and dissolution kinetics: implications for the thorium and light rare earth chemistry of felsic magmas. Contributions to Mineralogy and Petrology, 94, 304-316.

Rapp, J.F., Klemme, S., Butler, I.B., and Harley, S.L. (2010) Extremely high solubility of rutile in chloride and fluoride-bearing metamorphic fluids: An experimental investigation. Geology, 38, 323-326.

Rolland, Y., Cox, S., Boullier, A.-M., Pennacchioni, G., and Mancktelow, N. (2003) Rare earth and trace element mobility in mid-crustal shear zones: insights from the Mont Blanc Massif (Western Alps). Earth and Planetary Science Letters, 214, 203-219.

Schlüter, J., Malcherek, T., and Husdal, T.A. (2009) The new mineral stetindite, CeSiO4, a cerium end-member of the zircon group. Neues Jahrbuch für Mineralogie-Abhandlungen: Journal of Mineralogy and Geochemistry, 186, 195-200.

Schmidt, C., Rickers, K., Bilderback, D.H., and Huang, R. (2007) In situ synchrotron-radiation XRF study of REE phosphate dissolution in aqueous fluids to 800 °C. Lithos, 95, 87-102.

Seydoux-Guillaume, A.-M., Montel, J.-M., Bingen, B., Bosse, V., de Parseval, P., Paquette, J.-L., Janots, E., and Wirth, R. (2012) Low-temperature alteration of monazite: Fluid mediated coupled dissolution–precipitation, irradiation damage, and disturbance of the U–Pb and Th–Pb chronometers. Chemical Geology, 330-331, 140-158.

564 Skora, S., and Blundy, J. (2012) Monazite solubility in hydrous silicic melts at high pressure
565 conditions relevant to subduction zone metamorphism. Earth and Planetary Science
566 Letters, 321-322, 104-114.
567 Spear, F.S., and Pyle, J.M., (2002) Apatite, Monazite, and Xenotime in Metamorphic Rocks.
568 Reviews in Mineralogy and Geochemistry, 48, 293-335.
569 Stepanov, A.S., Hermann, J., Rubatto, D., and Rapp, R.P. (2012) Experimental study of
570 monazite/melt partitioning with implications for the REE, Th and U geochemistry of
571 crustal rocks. Chemical Geology, 300-301, 200-220.
572 Trail, D., Watson, E.B., and Tailby, N.D. (2012) Ce and Eu anomalies in zircon as proxies for the
573 oxidation state of magmas. Geochimica et Cosmochimica Acta, 97, 70-87.
574 Trail, D., Tailby, N.D., Lanzirotti, A., Newville, M., Thomas, J.B., and Watson, E.B. (2015) Redox
575 evolution of silicic magmas: Insights from XANES measurements of Ce valence in
576 Bishop Tuff zircons. Chemical Geology, 402, 77-88.
577 Tropper, P., and Manning, C.E. (2005) Very low solubility of rutile in H2O at high pressure and
578 temperature, and its implications for Ti-mobility in subduction zones. American
579 Mineralogist, 90, 502-505.
580 Tropper, P., Manning, C.E., and Harlov, D.E. (2011) Solubility of CePO4 monazite and YPO4
581 xenotime in H2O and H2O–NaCl at 800°C and 1GPa: Implications for REE and Y
582 transport during high-grade metamorphism. Chemical Geology, 282, 58-66.
583 Tropper, P., Manning, C.E., Harlov, D.E. (2013) Experimental determination of CePO4 and YPO4
584 solubilities in H2O-NaF at 800°C and 1 GPa: implications for rare earth element transport
585 in high-grade metamorphic fluids. Geofluids, 13, 372-380.

586 Veilly, E., Kerdaniel, E.d.F.d., Roques, J., Dacheux, N., and Clavier, N., (2008) Comparative
587 Behavior of Britholites and Monazite/Brabantite Solid Solutions during Leaching Tests:
588 A Combined Experimental and DFT Approach. Inorganic Chemistry, 47, 10971-10979.
589 Watson, E., Wark, D., Price, J., and Van Orman, J.A. (2002) Mapping the thermal structure of
590 solid-media pressure assemblies. Contributions to Mineralogy and Petrology, 142, 640-
591 652.
592 Whitfield, H.J., Roman, D., and Palmer, A.R., (1966) X-ray study of the system ThO2-CeO2-
593 Ce2O3. Journal of Inorganic and Nuclear Chemistry, 28, 2817-2825.
594 Williams, M.L., Jercinovic, M.J., Harlov, D.E., Budzyń, B., and Hetherington, C.J. (2011)
595 Resetting monazite ages during fluid-related alteration. Chemical Geology, 283, 218-225.
596 Xing, L., Trail, D., and Watson, E.B., (2013) Th and U partitioning between monazite and felsic
597 melt. Chemical Geology, 358, 46-53.
598
599
600
601
602
603
604
605
606
607
608

609

610 # Figure Captions

611

612

613 **Figure 1**. Capsule configurations and experimental cell. **(a)** The most common capsule
614 configuration separates the oxygen fugacity buffer from experimental sample by 0.15 mm thick
615 H_2 permeable Pd foil. Capsules are thick walled, to minimize the thermal gradient and to prevent
616 re-precipitation of the dissolved crystal though monazite is not prone to vapor-phase transport like
617 rutile (Tropper and Manning, 2005). **(b)** A fluid insoluble oxygen fugacity buffer (Ru-RuO_2) was
618 added directly to the capsule in a single experiment. **(c)** The capsule configuration used to buffer
619 the oxygen fugacity at the Ni-NiO equilibrium. This buffer was implemented in a similar fashion
620 to that described in Ayers et al. (1992). The Ni metal bucket was oxidized in a muffle furnace at
621 ~1000 ºC for 24 hours, and additional Ni-NiO powder and H_2O was added to the bottom of the Ni
622 bucket before inserting the 5 mm Pt capsule. **(d)** The experimental cell consists of a 19 mm NaCl+
623 borosilicate glass, with crushable MgO on either side of the capsule+buffer. No pressure
624 correction was made for this cell design (Holland, 1980). The borosilicate glass acts as a thermal
625 insulator; additional details about the thermal structure of the NaCl-borosilicate cell are explored
626 in Watson et al. (2002).

627

628

629 **Figure 2**. Solubility of Llallagua monazite in 2N NaOH solution represented as wt% monazite
630 dissolved in the fluid (wt. loss of crystal/ wt. of fluid×100). Solubilites increase at oxygen
631 fugacities above the FMQ buffer. The x-axis represents the difference in log units from the FMQ
632 equilibrium buffer. The iron-wüstite (IW) and magnetite-hematite (MH) buffers are included for
633 reference.

634

635 **Figure 3**. Solubility of monazite in 2N NaOH fluid compared to experiment duration for three
636 different oxygen fugacities, which reveals no systematic change with time, suggesting the absence
637 of vapor transport/recrystallization of dissolved solutes.

638

639 **Figure 4**. SEM images (SE = secondary electron; BSE backscattered electron) of Llallagua
640 monazite showing various types of dissolution features; see Table 1 for oxygen fugacity buffer
641 abbreviations. **(a)** Monazite experimental product buffered at MMO in 2N NaOH fluid showing
642 the presence of xenotime. Also present, but not shown in the image, are ~1 μm REE-silicates near
643 the surface of the crystal, likely allanite. Xenotime was not observed in any other experiment,
644 including other MMO runs and is suspected to have been present at the start of the experiment.
645 **(b)** MD16, also buffered at MMO. **(c)** Monazite experimental product after buffering at FMQ (2N
646 NaOH). **(d)** An experiment buffered at FMQ+2.8 with NaOH fluid shows evidence of incongruent
647 dissolution resulting in Ce-oxide precipitates close to the surface of the crystal. **(e)** Buffering the
648 experiment at RRO in a solution of 2N NaOH results in pervasive Ce-oxide associated with the
649 monazite at depths greater than 50 μm from the original surface of the crystal. **(f)** In contrast to
650 (e), no incongruent dissolution of monazite is evident at RRO in a fluid of H_2O.

651

652 **Figure 5.** Solubility of synthetic monazite crystals in 2N NaOH change as a function of chemical
653 composition. For reference, the grey line defines the solubility for natural monazite presented in
654 Figure 2. Synthetic $CePO_4$ exhibits enhanced solubilites at elevated oxygen fugacities. Synthetic
655 $LaPO_4$ and Th+Si doped monazite (see Table 2 for compositions) exhibit no change in solubility
656 as a function of oxygen fugacity. Error bars are smaller than the symbols.

Figure 6. SEM images of synthetic monazite crystals labeled with sample ID, fO_2 buffer, and image type (SE = secondary electron; BSE = backscattered electron). The first row are images of synthetic $CePO_4$, the second row is Si-Th doped monazites. **(a)** Flux-grown monazite, untreated. **(b)** Ce-oxide inclusions present on the surface of the crystal after an experiment buffered at FMQ. **(c-d)** Deep penetration of Ce-oxide after a RRO-buffered experiment; the surface was imaged first (c), followed by mounting and polishing of the crystal (d). **(e-g)** Precipitates of CeO_2-ThO_2 extending to depths of ~5 μm within the crystal, and on the surface. The CeO_2-ThO_2 phase is more prevalent for the more oxidized experiment (g), and has higher abundances of CeO_2 as determined by EDS.

This is a preprint, the final version is subject to change, of the American Mineralogist (MSA)
Cite as Authors (Year) Title. American Mineralogist, in press.
DOI: http://dx.doi.org/10.2138/am-2018-6296

678 **Table 1**
679

Table 1. Compositions of phosphates used in solubility experiments.

		(wt%)																	
Sample ID	n	Ca	1 s.d.	Si	1 s.d.	La	1 s.d.	Ce	1 s.d.	Pr	1 s.d.	Nd	1 s.d.	Sm	1 s.d.		Th	1 s.d.	U	1 s.d.
Llallagua grain 1	9	0.4	0.2	n.m.		19.0	0.9	33.4	1.1	3.4	0.2	12.3	1.1	1.8	0.2		101 ppm	303	404 ppm	681
Llallagua grain 2	10	0.6	0.2	n.m.		17.2	1.5	31.9	0.9	3.5	0.1	11.8	0.9	1.8	0.1		0.05 ppm	0.04	132 ppm	63
Llallagua grain 3	11	0.3	0.1	n.m.		18.2	0.8	31.9	0.7	3.3	0.0	12.9	0.3	1.7	0.1		0.04 ppm	0.12	291 ppm	194
Th-Si mzt (synth)	5			0.3	0.03	42.6	0.8	30.1	0.5	0.0	0.0	n.m.		n.m.			2.94 wt%	0.21	n.m.	
$LaPO_4$ (synth)	5			0.1	0.04	74.7	2.2	0.0	0.0	0.0	0.0	n.m.		n.m.			0.00 ppm	0.00		
$CePO_4$ (snyth)	5	b.d.l.		n.m.		0.0	0.0	76.4	1.3	0.0	0.0	0.0	0.0	n.m.			n.m.		b.d.l.	

n = number of analyses; additional spot data included in the supplementary information.

b.d.l = below detection limit

n.m. = not measured

680
681
682
683
684
685
686
687
688
689
690
691
692
693
694
695
696

This is a preprint, the final version is subject to change, of the American Mineralogist (MSA)
Cite as Authors (Year) Title. American Mineralogist, in press.
DOI: http://dx.doi.org/10.2138/am-2018-6296

Table 2

Table 2 solid state oxygen fugacity buffers used in this study.

fO_2 buffer equil. reaction	abbreviation, ref.	ΔFMQ	Capsule configuration
$Mo + O_2 = MoO_2$	Mo-MoO_2 (MMO), 1	-4.00	Fig 1(a)
$W + O_2 = WO_2$	W-WO_2 (WWO), 2	-2.70	Fig 1(a)
$[6/(4x-3)]FexO + O_2 = [2x/(4x-3)]Fe_3O_4$	WM, 3	-2.12	Fig 1(a)
$3Fe_2SiO_4 + O_2 = 2Fe_3O_4 + 3SiO_2$	**FMQ, 4**	**0.00**	**Fig 1(a)**
$2Ni + O_2 = 2NiO$	Ni-NiO (NNO), 2	0.80	Fig 1(c)
$Re + O_2 = ReO_2$	Re-ReO_2 (ReRO), 5	2.78	Fig 1(a)
$Ru + O_2 = RuO_2$	Ru-RuO_2 (RRO), 6	7.97	Fig 1(a,b)

[1]O'Neill (1986); [2]O'Neill and Pownceby (1993) ; [3]Myers and Eugster (1983);
[4]O'Neill (1987) ; [5]Pownceby and O'Neill (1994) ; [6]O'Neill and Nell (1997)

This is a preprint, the final version is subject to change, of the American Mineralogist (MSA)
Cite as Authors (Year) Title. American Mineralogist, in press.
DOI: http://dx.doi.org/10.2138/am-2018-6296

713 **Table 3**

Table 3 experiment conditions and results.

Exp ID	T (°C)	P (GPa)	capsuleconfig.	t(h)	fo_2	ΔFMQ	crystal type	fluid comp.	initial crystal wt. (mg)	fluid added (µL)	final crystal wt. (mg)	solubility (%) [a]	1 s.d. [b]
MD01	925	1.5	Fig 1a	70	RRO	7.97	Llallagua	2N NaOH	6.41	51	6.16	0.45	0.03
MD02	925	1.5	Fig 1a	70	FMQ	0.00	Llallagua	2N NaOH	4.15	33.2	4.08	0.20	0.03
MD03	925	1.5	Fig 1a	189	FMQ	0.00	Llallagua	2N NaOH	4.43	35.4	4.36	0.18	0.03
MD04	925	1.5	Fig 1a	24	FMQ	0.00	Llallagua	2N NaOH	10.01	40	9.93	0.19	0.03
MD06	925	1.5	Fig1b	24	RRO	7.97	Llallagua	2N NaOH	4.67	75	4.27	0.49	0.02
MD08	925	1.5	Fig 1a	46	WWO	-2.70	Llallagua	2N NaOH	4.86	45	4.77	0.19	0.02
MD09	925	1.5	Fig 1a	46	ReRO	2.78	$CePO_4$ (synth)	2N NaOH	8.94	45	8.27	1.38	0.02
MD10	925	1.5	Fig 1a	46	ReRO	2.78	Llallagua	2N NaOH	8.76	45	8.60	0.33	0.02
MD11	925	1.5	Fig 1a	48	WM	-2.12	Llallagua	2N NaOH	8.10	60	8.00	0.15	0.02
MD14	925	1.5	Fig 1a	48	MMO	-4.00	Llallagua	2N NaOH	13.25	60	13.17	0.12	0.02
MD15	925	1.5	Fig 1a	48	MMO	-4.00	$CePO_4$ (synth)	2N NaOH	2.50	60	2.40	0.15	0.02
MD16	925	1.5	Fig 1a	99	MMO	-4.00	Llallagua	2N NaOH	6.92	60	6.80	0.19	0.02
MD17	925	1.5	Fig 1a	48	FMQ	0.00	$CePO_4$ (synth)	2N NaOH	1.45	60	1.29	0.25	0.02
MD19	925	1.5	Fig 1a	48	RRO	7.97	$CePO_4$ (synth)	2N NaOH	6.37	60	4.69	2.59	0.02
MD20	925	1.5	Fig 1a	48	RRO	7.97	$LaPO_4$ (synth)	2N NaOH	4.77	60	4.66	0.17	0.02
MD21	925	1.5	Fig 1a	47	FMQ	0.00	$LaPO_4$ (synth)	2N NaOH	2.15	60	2.04	0.17	0.02
MD22	925	1.5	Fig 1a	48	RRO	7.97	Llallagua	H_2O	2.67	60	2.65	0.03	0.02
MD25	925	1.5	Fig 1a	46	RRO	7.97	Th-Si mzt (synth)	2N NaOH	5.47	60	5.37	0.15	0.02
MD28	925	1.5	Fig 1a	48	FMQ	0.00	Th-Si mzt (synth)	2N NaOH	3.83	60	3.73	0.15	0.02
MD34	925	1.5	Fig 1c	24	NNO	0.80	Llallagua	2N NaOH	3.76	60	3.58	0.28	0.02

[a] solubility represented as wt% monazite dissolved in the fluid (wt. loss of crystal/ wt. of fluid×100), using a density of 1.08 g/ml for 2N NaOH

[b] propagated uncertainty based on 3-7 repeated measurements of initial and final crystal weight

This is a preprint, the final version is subject to change, of the American Mineralogist (MSA)
Cite as Authors (Year) Title. American Mineralogist, in press.
DOI: http://dx.doi.org/10.2138/am-2018-6296

734
735 **Figure 1**

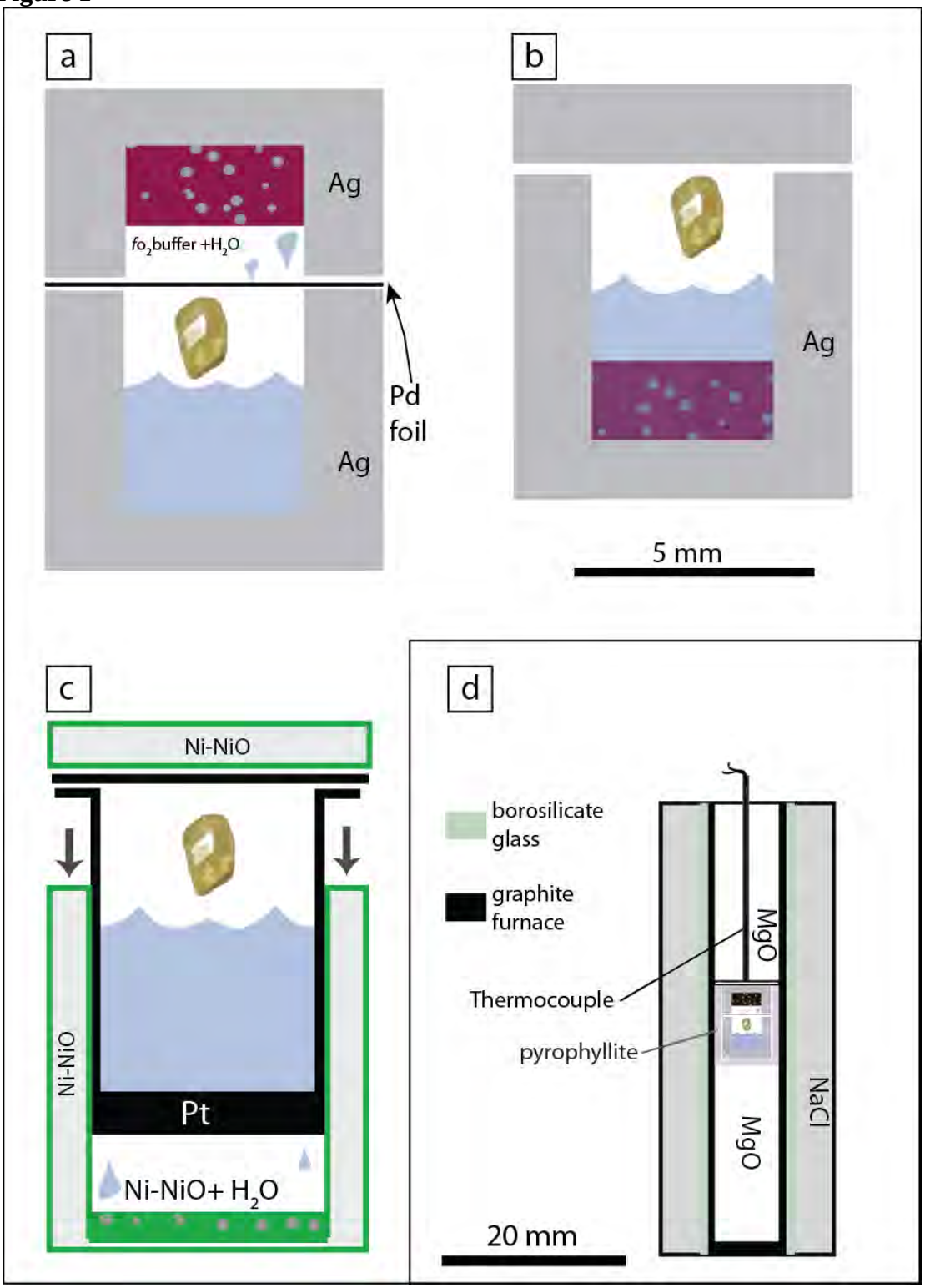

736
737

738

This is a preprint, the final version is subject to change, of the American Mineralogist (MSA)
Cite as Authors (Year) Title. American Mineralogist, in press.
DOI: http://dx.doi.org/10.2138/am-2018-6296

739 **Figure 2**

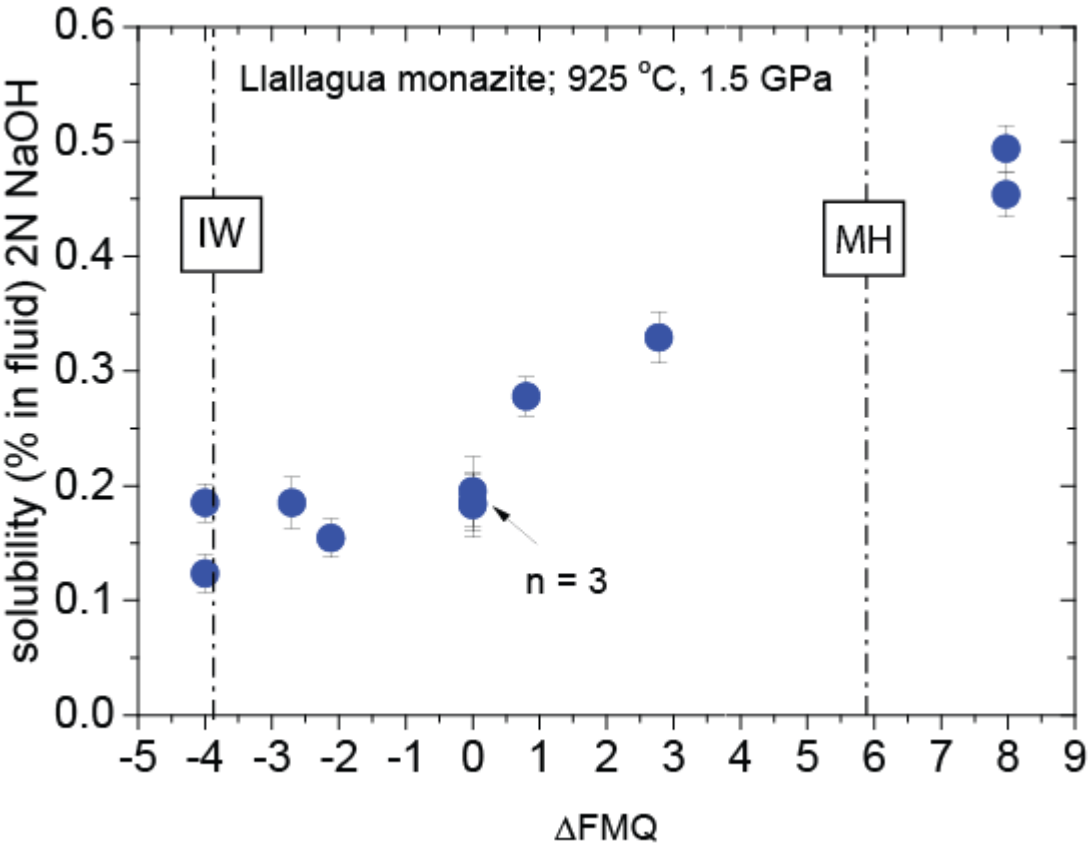

740

741

742

743

744

745

746

747

748

749

750

This is a preprint, the final version is subject to change, of the American Mineralogist (MSA)
Cite as Authors (Year) Title. American Mineralogist, in press.
DOI: http://dx.doi.org/10.2138/am-2018-6296

751 **Figure 3**

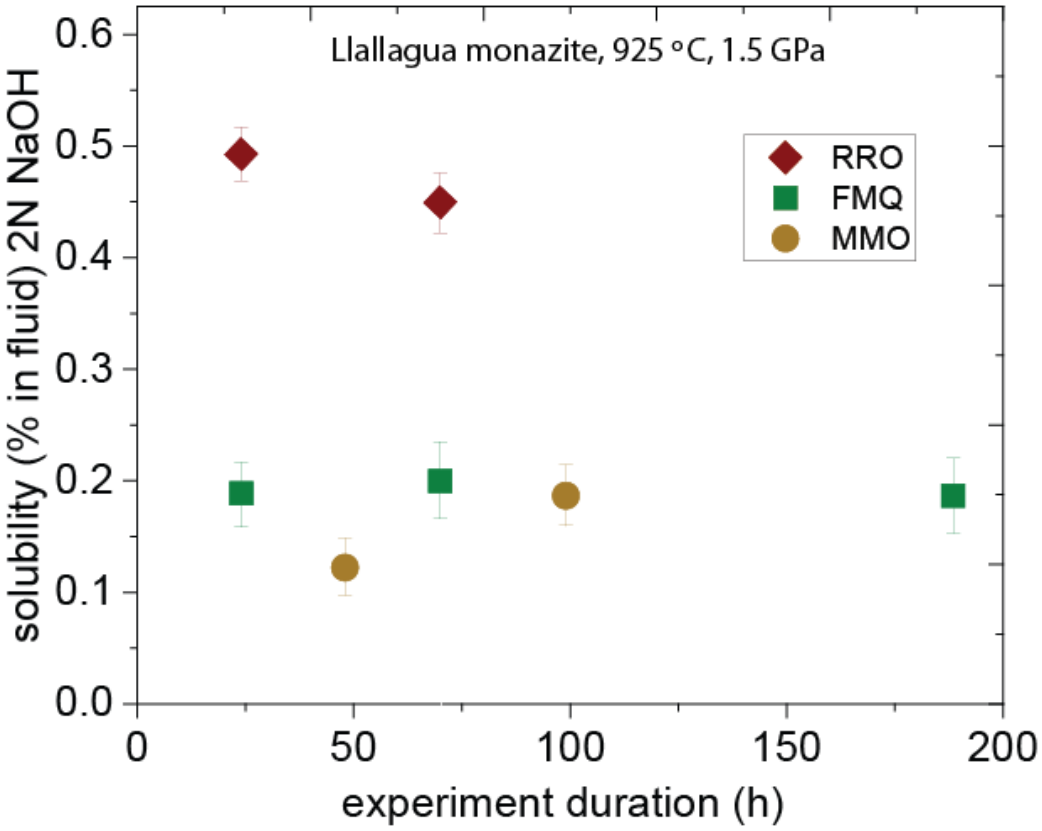

752

753

754

755

756

757

758

759

760

761

762

This is a preprint, the final version is subject to change, of the American Mineralogist (MSA)
Cite as Authors (Year) Title. American Mineralogist, in press.
DOI: http://dx.doi.org/10.2138/am-2018-6296

763 **Figure 4**

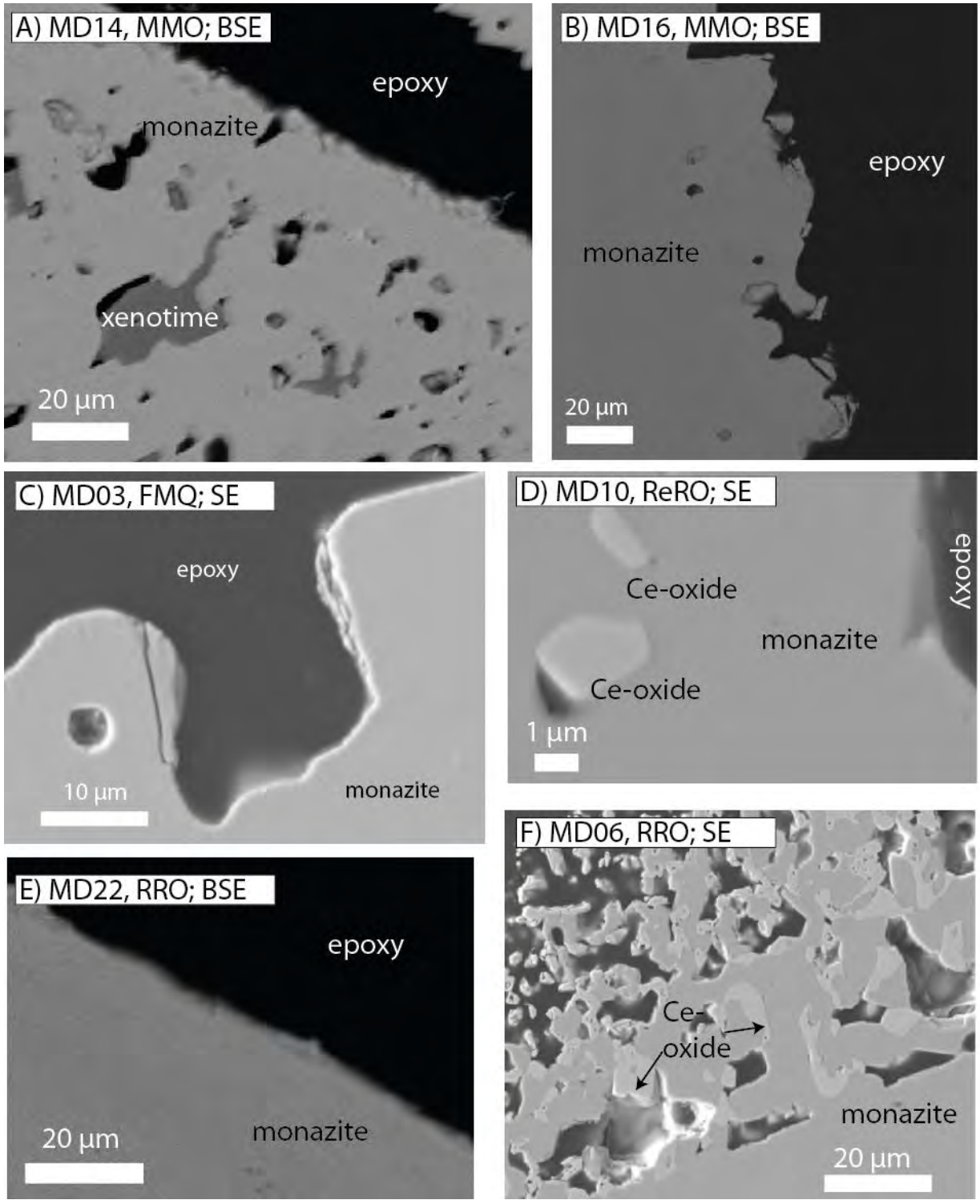

764

765

766

This is a preprint, the final version is subject to change, of the American Mineralogist (MSA)
Cite as Authors (Year) Title. American Mineralogist, in press.
DOI: http://dx.doi.org/10.2138/am-2018-6296

767 **Figure 5**

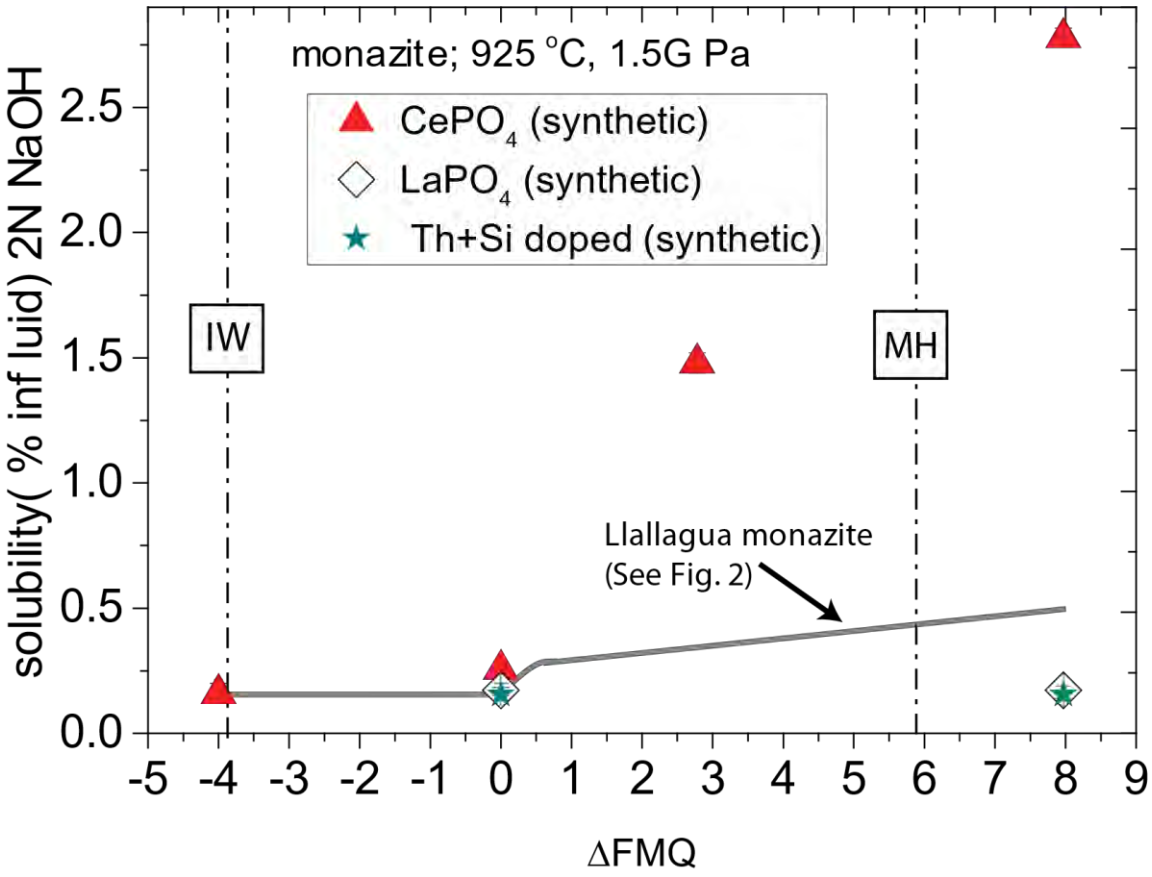

768

769

770

771

772

773

774

775

776

777

778

This is a preprint, the final version is subject to change, of the American Mineralogist (MSA)
Cite as Authors (Year) Title. American Mineralogist, in press.
DOI: http://dx.doi.org/10.2138/am-2018-6296

779 **Figure 6**

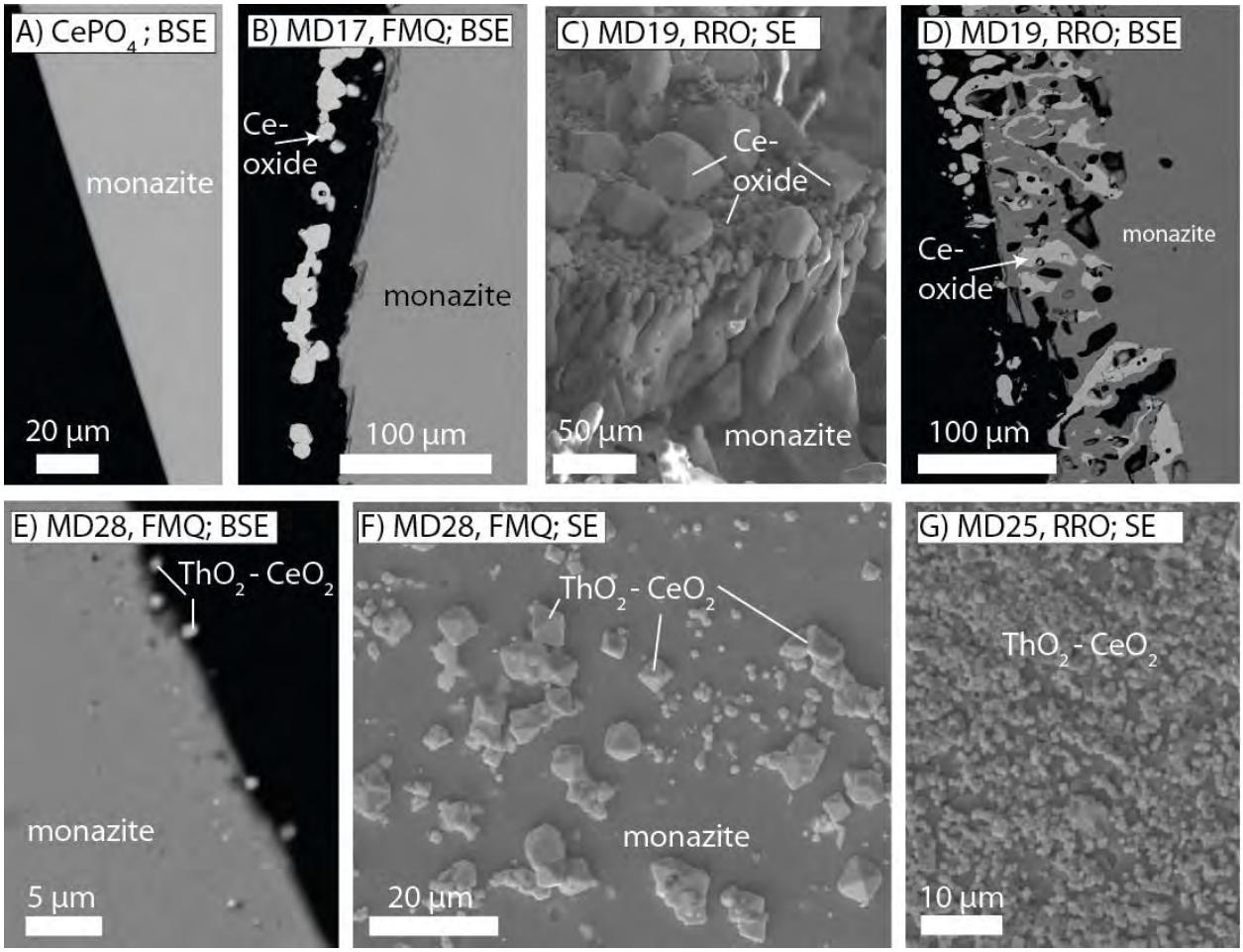

780

781
782
783
784